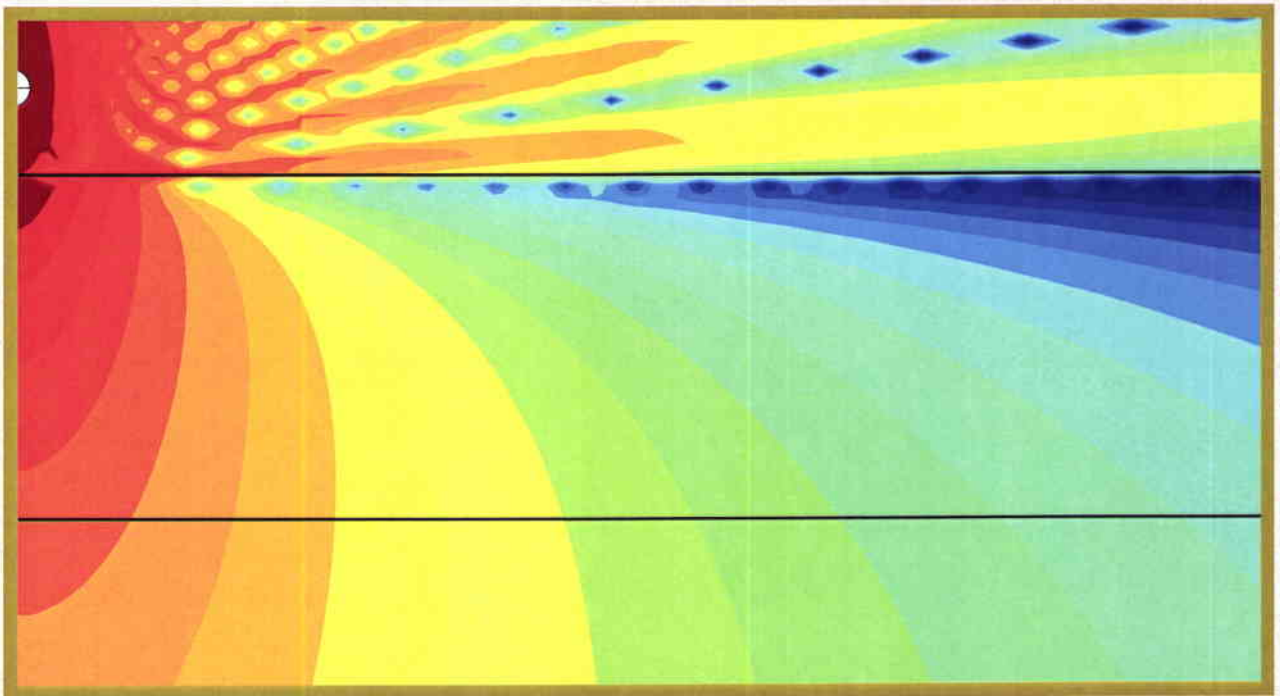


SACLANT UNDERSEA RESEARCH CENTRE REPORT



Spectral integral representations of monostatic
backscattering from three dimensional distributions
of sediment volume inhomogeneities



Kevin D. LePage and Henrik Schmidt

March 2001

SACLANTCEN SM-376

**Spectral integral representations
of monostatic backscattering from
three dimensional distributions of
sediment volume inhomogeneities**

Kevin D. LePage and Henrik Schmidt

The content of this document pertains
to work performed under Project 04-D of
the SACLANTCEN Programme of Work.
The document has been approved for
release by The Director, SACLANTCEN.



Jan L. Spoelstra
Director

intentionally blank page

SACLANTCEN SM-376

**Spectral integral representations
of monostatic backscattering from
three dimensional distributions of
sediment volume inhomogeneities**

Kevin D. LePage and Henrik Schmidt

Executive Summary: Sediment volume inhomogeneity scattering accounts for one type of reverberation against which sonar systems must discriminate targets in operational situations. In this report a model is described which can generate simulations of this type of reverberation for realistic bottom parameters and scatterer distributions. This new model provides a capability to provide reverberation estimates against which various target detection algorithms can be tested. The theoretical underpinnings of the model are described and the model is benchmarked for a simple situation against an existing raytrace solution. The new capabilities of the model are then highlighted by generating scattering simulations for more complicated situations where existing solutions are not available.

intentionally blank page

SACLANTCEN SM-376

**Spectral integral representations
of monostatic backscattering from
three dimensional distributions of
sediment volume inhomogeneities**

Kevin D. LePage and Henrik Schmidt

Abstract: A theory is developed for generating short time, monostatic reverberation realizations caused by three dimensionally distributed volume inhomogeneities in stratified media. A spectral integral approach to treating the propagation to and from the scatterers, combined with a two dimensional spectral representation of the azimuthally averaged scatterer realizations and a novel numerical implementation, combine to yield a efficient, high fidelity reverberation realization generator for predicting monostatic backscatter from realistic sediments.

Keywords: reverberation ◦ backscatter ◦ volume scattering ◦ seabed inhomogeneity

Contents

1	Introduction	1
2	Theory	3
	2.1 Monostatic backscatter	4
	2.2 Hankel Transform Evaluation	7
3	Results	10
	3.1 Scenario 1: Volume scattering from a slow sediment layer	12
	3.2 Scenario 2: Volume scattering from a fast sediment layer	15
	3.3 Scenario 3: Volume scattering from a upward refracting sediment layer	19
4	Conclusions	24
5	Acknowledgments	26
	References	27
	Annex A - Variance and covariance of Fourier-Bessel coefficients of scatterer distributions	30
	Annex B - Expressions for scattered intensity used by SCARAB	32

1

Introduction

The prediction of scattering from sediment volume inhomogeneities has been the subject of extensive study over the years [1–11,13,19]. Typically the sediment is treated as a homogeneous medium in which small perturbations in sound speed and density are superimposed. Due to the nature of the problem, predictions of scattered intensity are usually obtained under one or more subsequent approximations. When propagation is treated accurately, the perturbations are usually assumed to be uncorrelated vertically in order to pass through to expressions for the expected value of scattered intensity [3, 5]. If the propagation is simplified under the assumption that the scatterers are excited only by propagating waves, scattered intensity may also be obtained in closed form [6, 7]. If the interaction of the field with the scatterers is asymptotically evaluated, the full scattering of propagating and inhomogeneous waves may be evaluated for three dimensional distributions of scatterers, away from part of the sediment ensounded near the critical angle [9, 10]. However, if the propagation is to be treated “exactly” and a three dimensional distribution of scatterers is to be retained, then Monte-Carlo techniques for estimating the scattered intensity caused by sediment volume inhomogeneities are required. In a previous paper the authors laid out the theoretical basis for a unified treatment of sediment volume inhomogeneity scattering using spectral techniques [11]. In that paper the treatment of scattering from sound speed and density inhomogeneity scattering in general horizontally stratified acoustic media, including stratifications with background sound speed gradients, was presented for the two dimensional wave equation. In this paper we extend this spectral integral approach to treat laterally monostatic scattering in three dimensions.

Three dimensional scattering under the perturbation approximation is theoretically very similar to the two dimensional problem, especially in the fundamental equations. However the implementation is much more computationally demanding. The spectral integrals which must be evaluated for three dimensional problems are Fourier-Bessel transforms rather than Fourier transforms. For bistatic problems there is the requirement to evaluate $k_o r$ Fourier orders, where r is the bistatic separation between the source and the receiver, and k_o is the background sound speed [12, 14]. Finally, there is potentially a much larger number of contributing scatterers to be summed over to give the backscattered pressure, due to the addition of a dimension. For these reasons the generation of wave theoretic scattered field predictions for general bistatic geometries and scatterer distributions is a computa-

tionally demanding area which is just beginning to be explored [12, 13].

In this paper we take the first meaningful step towards a general three dimensional wave theoretic scatter prediction capability. We show that simplified expressions for backscatter may be obtained for laterally monostatic scenarios with horizontally isotropically distributed sediment inhomogeneities. In these cases the spectral integral representation of scattering from three dimensional sound speed fluctuations may still be obtained with one-dimensional integral transforms. The result is that a high fidelity computational capability for the generation of backscattering time series is obtained for relatively small cost over the previous two-dimensional implementation. Since the results are wave theoretic, the propagation is treated properly for general stratified acoustic media, even in the presence of background sound speed gradients. Propagation near the critical angle is treated properly for fast sediments, and propagation near turning points is treated properly for refractive sediments. And since the distribution properties of the inhomogeneities of the scatterers are intrinsically three dimensional, scattering from realistic scatterer distributions may be evaluated. The combination of these two factors and a unique numerical implementation introduces a new prediction capability into the field of sediment acoustics.

The first order scattered pressure observed at the field point $\{x, y, z\}$ due to small perturbation volume inhomogeneity scattering from sound speed perturbations $\Delta c/c$ in the depth interval $[z_1, z_2]$ is given by the convolution integral

$$p_s(x, y, z) = 2k_b^2 \int_{-\infty}^{\infty} dx' \int_{-\infty}^{\infty} dy' \int_{z_1}^{z_2} dz' G(\vec{r}, \vec{r}') \times \frac{\Delta c}{c}(x', y', z') p(x', y', z'), \quad (1)$$

where under the zeroth order Born approximation, p is the pressure incident on the scatterers in the absence of multiple scattering effects, $G(\vec{r}, \vec{r}')$ is the Green function from the scatterer at $\vec{r}' = (x', y', z')$ to the observer at $\vec{r} = (x, y, z)$, and the three-dimensional integral integrates over the space of contributing scatterers $\frac{\Delta c}{c}$. In a spectral integral modeling framework for a horizontally stratified medium, the Green function has the wavenumber integral representation [15]

$$G(r, z, z') = \int_0^{\infty} g(q_r; z, z') J_0(q_r r) q_r dq_r, \quad (2)$$

with $r = \sqrt{(x - x')^2 + (y - y')^2}$ representing the horizontal separation of scatterer and observer. $g(q_r; z, z')$ is the *depth-separated Green function* which, for example, in the case of a homogeneous background medium with acoustic wavenumber k_0 , can be derived as

$$g(q_r; z, z') = \frac{i}{4\pi} \frac{e^{i|z-z'|\sqrt{k_0^2 - q_r^2}}}{\sqrt{k_0^2 - q_r^2}}. \quad (3)$$

Similarly, for scatterers in a horizontally stratified ocean model, the incident acoustic pressure may be represented by a Fourier-Bessel integral

$$p(x', y', z') = \sum_{n=0}^{\infty} \left\{ \begin{array}{l} \cos n\theta' \\ \sin n\theta' \end{array} \right\} \int_0^{\infty} \tilde{p}_n(k_r, z') J_n(k_r r') k_r dk_r, \quad (4)$$

where $r' \equiv \sqrt{x'^2 + y'^2}$ and $\theta' \equiv \arccos(x'/r')$.

2.1 Monostatic backscatter

In the case of observations of scattering in a laterally monostatic geometry $x, y \equiv 0$, Eq. 1 considerably simplifies when the source is horizontally omnidirectional. Then the only non-zero Fourier harmonic in the source expansion is $n = 0$, and upon substitution of Eqs. 2 and 4, Eq. 1 may be written

$$\begin{aligned}
 p_s(z) &= 2k_b^2 \int_{-\infty}^{\infty} dx' \int_{-\infty}^{\infty} dy' \int_{z_1}^{z_2} dz' \frac{\Delta c}{c}(x', y', z') \\
 &\quad \times \int_0^{\infty} g(q_r; z, z') J_0(q_r r') q_r dq_r \\
 &\quad \times \int_0^{\infty} \tilde{p}_0(k_r, z') J_0(k_r r') k_r dk_r, \tag{5}
 \end{aligned}$$

or equivalently, converting to cylindrical coordinates and setting $\delta c \equiv \Delta c/c$,

$$\begin{aligned}
 p_s(z) &= 2k_b^2 \int_0^{\infty} r' dr' \int_{z_1}^{z_2} dz' \int_0^{2\pi} d\theta \delta c(r', \theta, z') \\
 &\quad \times \int_0^{\infty} g(q_r; z, z') J_0(q_r r') q_r dq_r \\
 &\quad \times \int_0^{\infty} \tilde{p}_0(k_r, z') J_0(k_r r') k_r dk_r. \tag{6}
 \end{aligned}$$

The angular integral in Eq. 6 indicates that the scattered field observed monostatically is averaged over non-dimensional sound speed perturbations δc in the cylindrical angle θ , yielding only a contribution from the zeroth order harmonic of the perturbations

$$\begin{aligned}
 \delta c_0(r, z') &\equiv \int_0^{2\pi} d\theta \delta c(r, \theta, z') \\
 &= \int_0^{\infty} \tilde{\delta c}_0(p_r, z') J_0(p_r r) p_r dp_r. \tag{7}
 \end{aligned}$$

By definition the spatial distribution of scatterers is related to its complex spectrum through the Fourier integral

$$\delta c(x, y, z') = \int_{-\infty}^{\infty} \int_{-\infty}^{\infty} \tilde{\delta c}(k_x, k_y, z') e^{ik_x x} e^{ik_y y} dk_x dk_y, \tag{8}$$

which may be expressed in cylindrical coordinates as

$$\begin{aligned}
 \delta c(r, \theta, z') &= \int_{-\infty}^{\infty} \int_{-\infty}^{\infty} \tilde{\delta c}(k_x, k_y, z') e^{ik_x r \cos \theta} e^{ik_y r \sin \theta} dk_x dk_y \\
 &= \int_0^{\infty} p'_r dp'_r \int_0^{2\pi} d\theta' \tilde{\delta c}(p'_r \cos \theta', p'_r \sin \theta', z') e^{ip'_r r \cos \theta' \cos \theta} e^{ip'_r r \sin \theta' \sin \theta}
 \end{aligned}$$

SACLANTCEN SM-376

The n^{th} Fourier harmonic of the Fourier-Bessel transformation of $\delta c(r, \theta)$ is defined by the relation

$$\tilde{\delta c}_n(p_r, z') = \int_0^\infty J_n(p_r r) r dr \int_0^{2\pi} d\theta \left\{ \begin{array}{c} \cos n\theta \\ \sin n\theta \end{array} \right\} \delta c(r, \theta, z'). \quad (10)$$

For monostatic backscatter the form of Eqs. 6 and 7 suggests that only the $n \equiv 0$ order Fourier-Bessel transform of the perturbation δc is required. Insertion of Eq. 9 into Eq. 10 for $n = 0$ yields

$$\begin{aligned} \tilde{\delta c}_0(p_r, z') &= \int_0^{2\pi} d\theta \int_0^{2\pi} d\theta' \int_0^\infty r dr \int_0^\infty J_0(p_r r) p'_r dp'_r \\ &\times \tilde{\delta c}(p'_r \cos \theta', p'_r \sin \theta', z') e^{ip'_r r \cos \theta' \cos \theta} e^{ip'_r r \sin \theta' \sin \theta}. \end{aligned} \quad (11)$$

Equation 11 may be simplified through the variable transformation

$$\theta' = \theta + \theta'',$$

which yields

$$\begin{aligned} \cos \theta' &= \cos(\theta + \theta'') = \cos \theta \cos \theta'' - \sin \theta \sin \theta'', \\ \sin \theta' &= \sin(\theta + \theta'') = \sin \theta \cos \theta'' + \cos \theta \sin \theta''. \end{aligned}$$

In this case the complex exponentials in Eq. 11 may be considerably simplified as

$$e^{ip'_r r \cos \theta' \cos \theta} e^{ip'_r r \sin \theta' \sin \theta} \equiv e^{ip'_r r \cos \theta''}, \quad (12)$$

so that Eq. 11 may be written

$$\begin{aligned} \tilde{\delta c}_0(p_r, z') &= \int_0^\infty J_0(p_r r) r dr \int_0^\infty p'_r dp'_r \int_0^{2\pi} d\theta \int_{-\theta}^{2\pi-\theta} d\theta'' \\ &\times \tilde{\delta c}(p'_r \cos(\theta + \theta''), p'_r \sin(\theta + \theta''), z') e^{ip'_r r \cos \theta''} \\ &= \int_0^\infty J_0(p_r r) r dr \int_0^\infty p'_r dp'_r \int_0^{2\pi} d\theta''' \tilde{\delta c}(p'_r \cos \theta''', p'_r \sin \theta''', z') \\ &\times \int_0^{2\pi} d\theta \cos(p'_r r \cos(\theta''' - \theta)). \end{aligned} \quad (13)$$

The integral over θ in Eq. 13 is evaluated as the Bessel function $2\pi J_0(p'_r r)$. If $\tilde{\delta c}(k_x, k_y, z')$ is isotropic and composed of $p'_r/2\pi$ independent normal distributed random variables of variance $P_{\delta c}(p'_r)$, where $P_{\delta c}$ is the power spectrum of the perturbations δc , then the integral over θ''' may be evaluated (see Annex A for details) with the result

$$\int_0^{2\pi} \tilde{\delta c}(p'_r \cos \theta''', p'_r \sin \theta''', z') d\theta''' = N(0, 2\pi P_{\delta c}(p'_r, z')/p'_r), \quad (14)$$

where $N(0, 2\pi P_{\delta c}(p'_r, z')/p'_r)$ is a normal distributed random variable with variance $\sigma^2 = 2\pi P_{\delta c}(p'_r, z')/p'_r$. Thus Eq. 13 may be evaluated with the result

$$\tilde{\delta}_{c0}(p_r, z') = 2\pi \int_0^\infty J_0(p_r r) r dr \int_0^\infty dp'_r \sqrt{p'_r} N(0, 2\pi P_{\delta c}(p'_r, z')) J_0(p'_r r), \quad (15)$$

so that by the Fourier-Bessel transform relation

$$\tilde{\delta}_{c0}(p_r, z') = 2\pi N(0, 2\pi P_{\delta c}(p_r, z')/p_r). \quad (16)$$

Insertion of Eq. 16 into Eq. 7 then yields the azimuth averaged perturbation realization

$$\delta_{c0}(r', z') = 2\pi \int_0^\infty J_0(p_r r') dp_r \sqrt{2\pi p_r} N(0, P_{\delta c}(p_r, z')).$$

Equation 6 then takes the form

$$\begin{aligned} p_s(z) &= 4\pi \sqrt{2\pi} k_b^2 \int_0^\infty r' dr' \int_{z_1}^{z_2} dz' \int_0^\infty \sqrt{p_r} N(0, P_{\delta c}(p_r, z')) J_0(p_r r') dp_r \\ &\times \int_0^\infty g(q_r; z, z') J_0(q_r r') q_r dq_r \\ &\times \int_0^\infty \tilde{p}_0(k_r, z') J_0(k_r r') k_r dk_r. \end{aligned} \quad (17)$$

Changing the orders of integration, Eq. 17 can be cast into a form which is directly suited for implementation in a wavenumber integration modeling framework for ocean waveguides,

$$\begin{aligned} p_s(z) &= 4\pi \sqrt{2\pi} k_b^2 \int_0^\infty q_r dq_r \int_{z_1}^{z_2} dz' g(q_r; z, z') \int_0^\infty J_0(q_r r') r' dr' \\ &\times \int_0^\infty \sqrt{p_r} N(0, P_{\delta c}(p_r, z')) J_0(p_r r') dp_r \\ &\times \int_0^\infty \tilde{p}_0(k_r, z') J_0(k_r r') k_r dk_r. \end{aligned} \quad (18)$$

In this form the two inner integrals are uncoupled and may be evaluated directly a priori for a selected grid of scatterers in the spatial (r', z') domain. The integral over k_r represents the incident pressure field, while the integral over p_r represents the cylindrically averaged scattering strength at (r', z') . The product of these integrals then represents the horizontal distribution of virtual sources at depth z' contributing to the scattered field. The Hankel transform integral over r' converts this sheet of virtual sources into an equivalent wavenumber spectrum, which multiplied by the depth-dependent Green function represents the generated scattered field component at horizontal wavenumber q_r . The depth integral then superimposes the contributions from all scatterer depths to produce the total kernel of the Hankel wavenumber integral for the monostatic reverberant field on the coordinate axis $r = 0$, which is evaluated using any of the standard wavenumber integration techniques [15].

SACLANTCEN SM-376

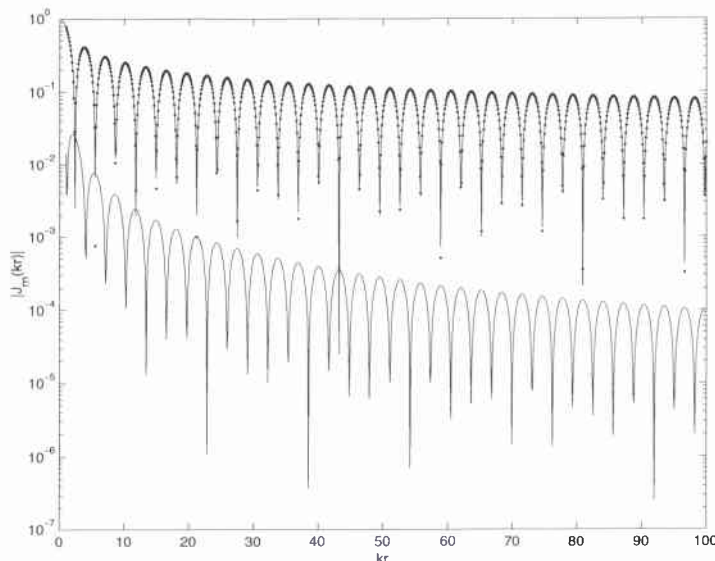


Figure 1 Error of far-field approximation of $J_0(kr)$. Solid: Exact. Dots: Large-argument approximation, Dashed: Error.

2.2 Hankel Transform Evaluation

In underwater acoustic modeling the Hankel transform wavenumber integrals have traditionally been evaluated using the so called Fast Field Program (FFP) approach [21], which is based on the large argument asymptotic of the Hankel functions. However, for the ocean reverberation problem this approach is inadequate because of the significance of the steep angle contributions from scatterers at short range. Even on today's computers the generation of Bessel functions is time consuming, and a direct numerical quadrature technique for evaluating the Hankel transforms in Eq. (18) is infeasible. A number of *Fast Hankel Transforms* have been developed [22, 23, 24], but they are in general restrictive in terms sampling requirements and therefore not easily adapted to the ocean acoustics problem where the sampling is controlled by the waveguide physics, and where the field is desired at a predetermined grid of horizontal ranges. Being based on the FFT, the advantage of the FFP is that it efficiently approximates the Hankel transform on a regular grid of wavenumbers and ranges. However, it is possible to design a numerically efficient correction to the FFP which allows for accurate accounting for the small argument contributions.

The Hankel transform integrals are of the form

$$\begin{aligned}
 f(r) &= \int_0^{\infty} f(k)k J_m(kr) dk \\
 &= \frac{1}{2} \int_0^{\infty} f(k)k \left[H_m^{(1)}(kr) + H_m^{(2)}(kr) \right] dk
 \end{aligned} \tag{19}$$

where $H_m^{(1)}$ for $\exp -i\omega t$ time-dependence corresponds to outgoing waves and $H_m^{(2)}$ to incoming waves, both of azimuthal Fourier order m dependence. For classical acoustic forward propagation modeling the incoming waves are ignored, eliminating the second term. However, for the backscattering problem it must be retained. Next the Hankel functions $H_m^{(1,2)}(k_r r)$ by their asymptotic form [25],

$$\lim_{kr \rightarrow \infty} H_m^{(1,2)}(k_r r) = \sqrt{\frac{2}{\pi k_r r}} e^{\pm i[k_r r - (m + \frac{1}{2})\frac{\pi}{2}]}, \quad (20)$$

to arrive at the following approximation to the Hankel transform,

$$f^*(r) = \sqrt{\frac{1}{2\pi r}} \int_0^\infty f(k) \sqrt{k} \left[e^{i[kr - (m + \frac{1}{2})\frac{\pi}{2}]} + e^{-i[kr - (m + \frac{1}{2})\frac{\pi}{2}]} \right] dk \quad (21)$$

This integral can be rewritten as a two-sided Fourier transform,

$$f^*(r) = \int_{-\infty}^\infty g(k) e^{ikr} dk, \quad (22)$$

with the kernel

$$g(k) = \begin{cases} f(-k) \sqrt{\frac{-k}{2\pi r}} e^{i(m + \frac{1}{2})\frac{\pi}{2}} & k < 0 \\ f(k) \sqrt{\frac{k}{2\pi r}} e^{-i(m + \frac{1}{2})\frac{\pi}{2}} & k \geq 0 \end{cases} \quad (23)$$

The Fourier transform is efficiently evaluated using a standard Fast Fourier Transform if the range r and wavenumber k are discretized equidistantly, with the sampling intervals being constrained by

$$\Delta r \Delta k_r = \frac{2\pi}{M}, \quad (24)$$

where M is an integral power of 2.

The error associated with using Eq. (22) is clearly associated with the approximation of the Bessel function in terms of the asymptotic expressions of the Hankel functions. Figure 1 shows the exact value of the absolute value of the Bessel function $J_0(kr)$ for $kr \leq 100$ as a solid curve and the asymptotic values indicated by the dots. The absolute error is indicated by the dashed curve, and it is clear that the relative error of the approximation is less than 10^{-5} for $kr \leq 20\pi$. Consequently, to achieve a more accurate evaluation of the Hankel Transforms of order 0 in Eq. (18) it is only necessary to correct the contributions corresponding values of $kr \leq KR = 20\pi$. This is performed in a numerically stable manner by a Hanning weighted average of the contributions of the exact Bessel function and the approximate FFP kernel,

$$\begin{aligned} f(r) &= f^*(r) \\ &+ \int_0^\infty f(k) w(kr) k J_0(kr) dk \\ &- \int_0^\infty f(k) w(kr) \sqrt{\frac{k}{2\pi r}} \left[e^{i(kr - (m + \frac{1}{2})\frac{\pi}{2})} + e^{-i(kr - (m + \frac{1}{2})\frac{\pi}{2})} \right] dk \quad (25) \end{aligned}$$

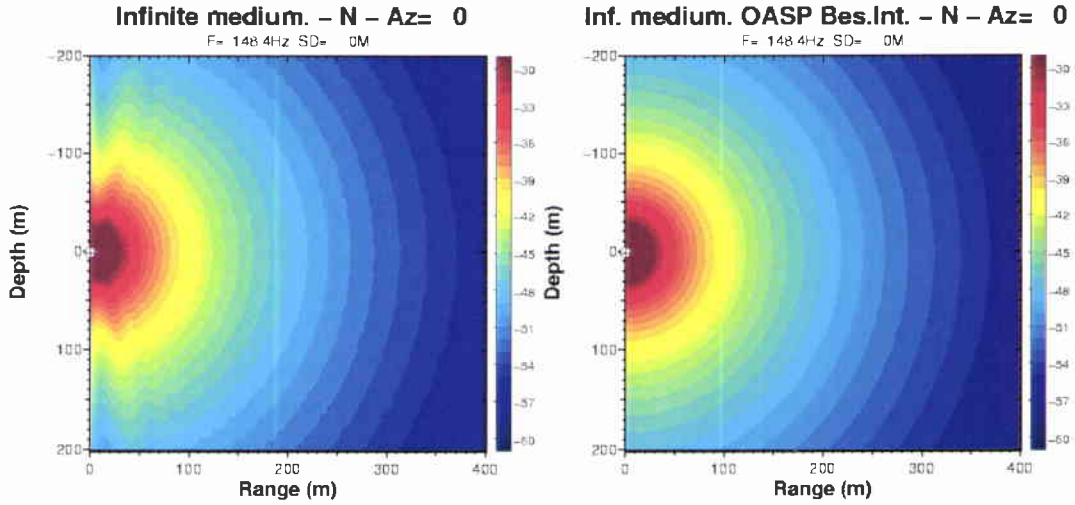


Figure 2 Acoustic point source field. (a) shows the FFP approximation which clearly breaks down at steep angles and short ranges, while (b) shows the correct spherical spreading behavior at all propagation angles, produced using Eq. (25)

where the tapered weight function $w(kr)$ is

$$w(kr) = \begin{cases} 1 & kr \leq KR/2 \\ [1 + \cos(\pi(kr - KR/2)/(KR/2))]/2 & KR/2 < kr < KR \\ 0 & kr \geq KR \end{cases} \quad (26)$$

Equation (25) can be evaluated very efficiently. First of all, with the wavenumber and range sampling constrained by Eq. (24), all values of the exponentials are computed as part of the FFT evaluation of Eq. (21). Secondly, the Bessel functions will only be needed for a limited number of discrete values of the argument,

$$kr = n\Delta k\Delta r, \quad n = 0, \dots, KR/(\Delta k\Delta r), \quad (27)$$

which can be precomputed into a look-up table.

The performance of this 'Fast Hankel Transform' is illustrated by Fig. 2, which shows the evaluation of the Hankel transform

$$p(r, z) = \int_0^\infty \frac{e^{ik_z|z|}}{ik_z} k J_0(kr) dk \quad (28)$$

representing the free-field point source field. $k_z = \sqrt{(\omega/c)^2 - k^2}$ is the vertical wavenumber at angular frequency ω . Figure 2(a) shows the FFP approximation which clearly breaks down at steep angles and short ranges, while Fig. 2(b) shows the correct spherical spreading behavior at all propagation angles produced using Eq. (25).

3

Results

Using the FHT outlined in Eq. 25, Eq. 18 and its wave theoretic equivalent for scattering from density inhomogeneities [11] has been implemented inside the OASES [17] code in a numerically efficient way. In the algorithm, the code is first run to generate the incident field through the scattering volume, as indicated by the third line of Eq. 18. Under the zeroth order Born approximation this field is assumed to be unaffected by the scattering process. This incident field is then modulated in the spatial domain by the azimuthally averaged scatterer distributions at each range and depth, as shown by the second line in Eq. 18. The resulting virtual source distribution at each scattering depth is then transformed to the scattered wavenumber domain. This gives the spectral distribution of the right-hand-side of the inhomogeneous depth-separated wave equation for the scattered field. The source spectrum for the scattered field at each scatterer depth is essentially a more complicated version of a point source expansion, since there is now an array of point sources at each depth whose strengths depend both on the incident field and the distribution properties of the scatterers.

The resulting inhomogeneous depth separated wave equation for the scattered field is solved using the *Global Matrix* approach [17]. The result is the spatial distribution of the scattered field for the desired frequency. To generate scattered field time series, Eq. 18 must be solved over an array of frequencies for the same scatterer distribution. Thus the second line of Eq. 18 is evaluated once for the scatterer distribution and then is modulated against the incident field at each frequency of interest in order to determine the virtual source representation. The resulting frequency dependent source term is then used to drive the depth separated wave equation for the scattered field, which is also frequency dependent, over the desired frequency band. The result is a complex transfer function between the incident field which was used to determine the third line of Eq. 18 and the scattered field at the desired horizontally monostatic receiver depths z .

The complex scattered field transfer functions may be used to synthesize scattered field time series in the usual manner. The sampling requirements of the scattered field time series must be in harmony with those of the spatial sampling of the scatterer realization and the incident field. In practice the spatial integrals on the second and third lines of Eq. 18 are truncated at a range sufficient to give scattered returns from all times of interest in the temporal Fourier synthesis. For instance for

SACLANTCEN SM-376

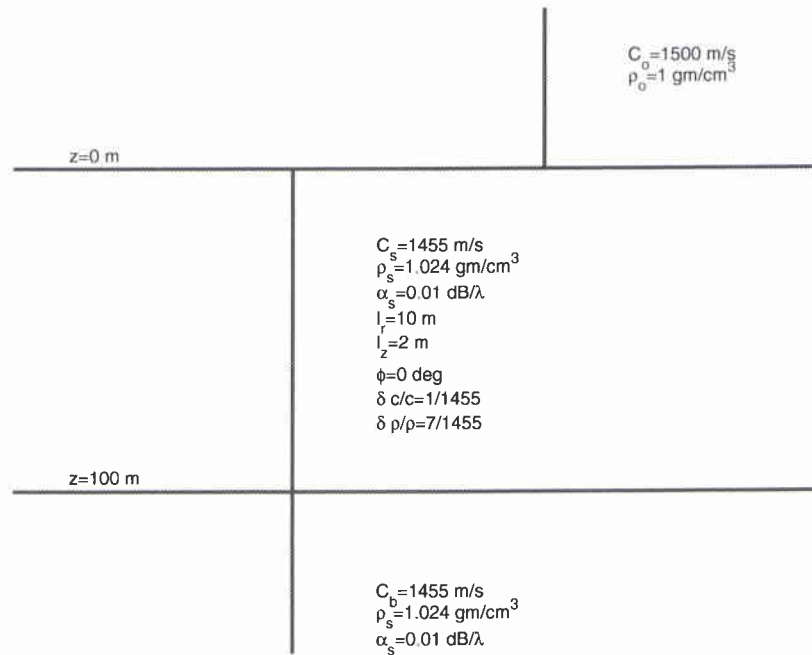


Figure 3 Sound speed profile and scatterer properties of volume scattering Scenario 1. An isospeed halfspace overlies a slow sediment layer 100 m thick with a background sound speed of 1455 m/s and density of 1.024 g/cm³. The basement halfspace has identical properties. In the scattering layer there are 100% correlated sound speed and density inhomogeneities conforming to a power law distribution with a fractal dimension of 3.5. The rms sound speed fluctuation is 1 m/s and the density fluctuation is 7/1455 g/cm³. The horizontal correlation length scales of the scatterers is 10 m and the vertical correlation length scale is 2 m. The high frequency asymptote of the scatterer distribution power spectrum is $k^{-7/2}$.

a 1 Hz sampling interval, scatterers up to a range of roughly 750 m are expected to contribute to the scattered field time series at the 1 s upper limit of the corresponding temporal window of the time series. In addition, the spatial sampling interval must be sufficiently fine to properly excite backscattered waves, which means that the maximum spatial sampling interval which is possible is one half a wavelength. Since the scatterer realization is generated once, this criteria is required to be satisfied at the upper end of the frequency band of interest. In practice the spatial sampling is also required to be smaller than the correlation length scale of the scatterers.

3.1 Scenario 1: Volume scattering from a slow sediment layer

Scattered field time series evaluated by Fourier synthesis of Eq. 18 have been generated for three scattering scenarios. Scenario 1 is illustrated in Figure 3. A point source is situated 25 m above a slow sediment layer 100 m thick with a background sound speed of 1455 m/s, a background density of 1.024 g/cm³ and an intrinsic attenuation of 0.01dB/λ. In the sediment layer there is a distribution of sound speed and density fluctuations which are 100% correlated. The rms amplitude of the sound speed fluctuations is 1 m/s, while the rms density fluctuation is 7/1455 g/cm³. The fluctuations are distributed according to a power law with a lateral correlation length scale $\ell_x = \ell_y = 10$ m and a vertical correlation length scale $\ell_z = 2$ m. The scatterer power spectrum has the form

$$P_{\delta c}(k_r, k_z) = \langle \delta c^2 \rangle \frac{\ell_r^2 \ell_z \Gamma(1.75)}{\pi^{1.5} \Gamma(.25)} \left(1 + k_r^2 \ell_r^2 + k_z^2 \ell_z^2 \right)^{-1.75} \quad (29)$$

which corresponds to a three dimensional von Karman [19] spectrum with fractal dimension 3.5 [20].

In all the scenarios, the properties of the basement are identical to the background properties of the sediment layer. This is not a requirement of the implementation, which can indeed insert a volume scattering layer into an arbitrary horizontally stratified waveguide, but rather a choice which tends to make the benchmarking and explanation of the results more straightforward.

In Figure 4 the absolute value of the complex envelope of the scattered field time series received on an array of receivers at the origin are shown in a stacked format for a particular realization of sediment inhomogeneities. The source pulse is Gaussian shaded with a center frequency of 500 Hz and a bandwidth of 20 Hz. The results show that the receivers closest to the sediment water interface receive the scattered field first, with the slope of the first arrival at higher receivers corresponding to the sound speed in the upper half space.

To further interpret the scattered field predictions it is useful to beamform the scattered field received on the vertical line array to transform the results to the time-angle domain. The resulting time-beam evolution of scattered field intensity, averaged over 16 independent scatterer realizations conforming to the distribution properties in Eq. 29, is shown in the lower panel of Figure 5. In the upper panel an independent estimate of the beam-time evolution of backscatter intensity obtained with the ray trace code SCARAB [7, 8] is shown for purpose of comparison. In the spectral integral representation the source pulse has a peak level of 1 μPa @ 1 m and is Gaussian shaded with a bandwidth of 20 Hz. In the SCARAB implementation the source pulse window is a rectangle of uniform amplitude of 1 μPa @ 1 m and duration $T = 5$ ms. The spectral results have been adjusted to correct for the

SACLANTCEN SM-376

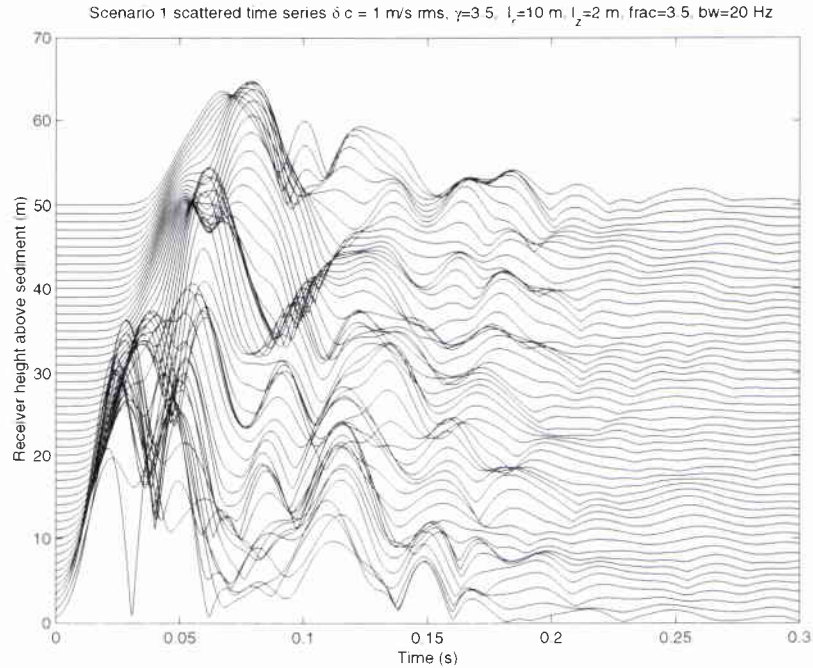


Figure 4 Scenario 1 stacked scattered field time series. The absolute value of the complex envelope of the field received over a 50 m aperture array of receivers as a function of time after the source pulse. The source pulse is Gaussian shaded with a center frequency of 500 Hz and a bandwidth of 20 Hz.

differences in incident energy between these two source pulses. The incident energy in the SCARAB source pulse is

$$\begin{aligned} E_{SCARAB} &= \int_0^T \cos^2(i\omega_0 t) dt \\ &= T/2, \end{aligned} \quad (30)$$

while for the spectral integral with the Gaussian shaded source pulse it is

$$\begin{aligned} E_{OASES} &= \int_{-\infty}^{\infty} \left(\cos(i\omega_0 t) e^{-(\omega - \omega_0)^2 / 2\Delta\omega^2} \right)^2 dt \\ &= \sqrt{\pi}/2 \Delta\omega. \end{aligned} \quad (31)$$

With the normalization of the spectral integral results it is possible to directly compare the scattered field intensity received by a single hydrophone with the SCARAB results. The results are shown in Figure 6 for a receiver at the source depth of 25 m above the sediment-water interface. In general the agreement between the two results is quite good, within 1 or 2 dB over that range of times and angles.

The agreement between the spectral integral and SCARAB representations of the scattered field intensity is satisfying because the differences between Eq. 18 and the

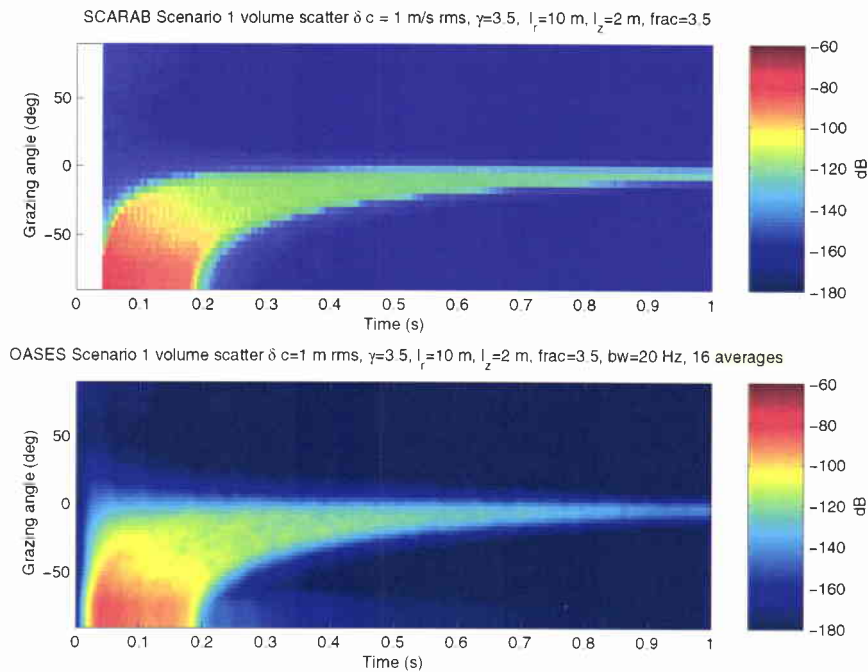


Figure 5 *The beam-time evolution of volume scattering intensity predicted by SCARAB (upper plot) and the spectral integral implementation discussed in this paper (lower plot.) In the spectral integral approach, time series are collected and beamformed on an array with a 50 m aperture at the origin whose center is collocated at the source depth. The beamformed results are then squared and averaged over an ensemble of 16 independent realizations of the sediment inhomogeneities to give an estimate of the expected value of the scattered intensity. Good agreement is seen between the two approaches, with the scattered intensity falling between the time-angle trajectories of scatterers at the top and bottom of the sediment layer. Note that the beamforming of the spectral integral results introduces some sidelobes. The SCARAB results have no sidelobes because they are obtained directly in the time-angle domain.*

sonar type equation for RL in the SCARAB manual are quite significant (for convenience, a short description of the SCARAB model is given in Annex B.) While both models use the Born approximation and first order perturbation theory, both the Green functions and the scattering are treated differently in practice. SCARAB has a ray trace approximation for the Green function while the spectral integral implementation accurately models the total Green function, including evanescent waves and propagation near the critical angle for fast bottoms. For scattering SCARAB integrates the differential planewave scattering cross-section of the sediment inhomogeneities over the sediment volume to estimate the scattered intensity, while the spectral integral calculates the scattered pressure from each scatterer over a particular realization of scatterers. In this case, the expected value of the scattered intensity is estimated by Monte-Carlo averaging the square of the scattered pressure

SACLANTCEN SM-376

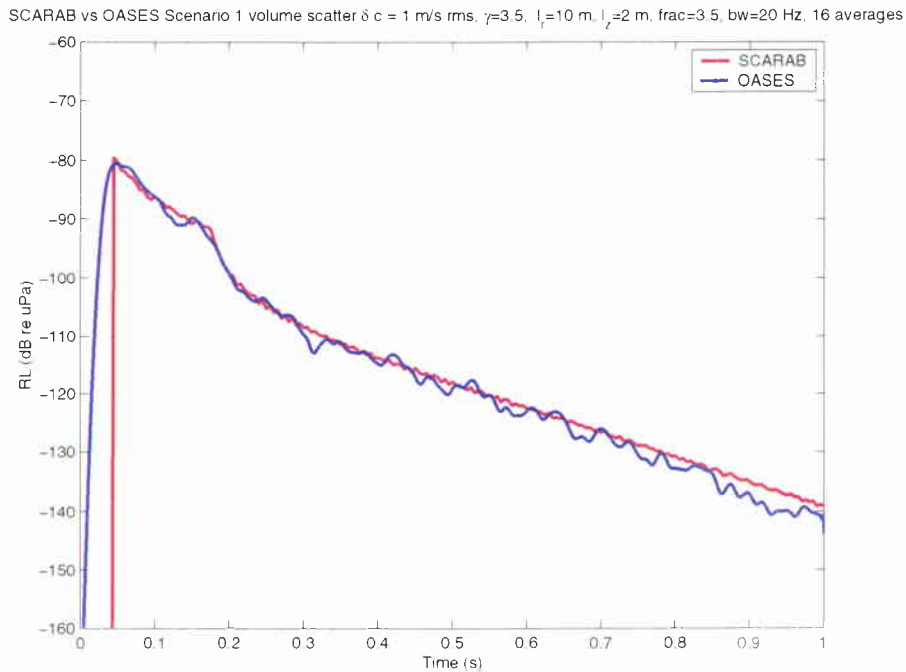


Figure 6 Single phone scattered field intensity estimates from SCARAB (red) and the current implementation (blue.) The spectral integral estimates of the scattered pressure have been squared and averaged over 16 independent realizations of the sediment layer inhomogeneities. Agreement with the SCARAB results is quite good, typically within 1 or 2 dB.

over an ensemble of scatterer realizations. Finally, the expression SCARAB uses for the differential cross-section, Eq. (42) from Yamamoto [6], also does not require the gradient of the scatterer distribution or of the incident field, as do the density scattering contributions in the spectral integral representation [11]. Thus the good agreement between the SCARAB and the spectral integral results lends confidence that Eq. 18 and the numerical implementation are consistent with the sonar equation approach to describing the sediment inhomogeneity scattering process for slow bottoms. As discussed below, we expect the two approaches to be equivalent only in cases where the sediment scattering process is well described by a plane wave differential scattering cross section and where the propagation is well approximated by ray theory.

3.2 Scenario 2: Volume scattering from a fast sediment layer

One significant advantage of using the spectral integral approach to modeling sediment volume inhomogeneity scattering is that the Green function is accurately mod-

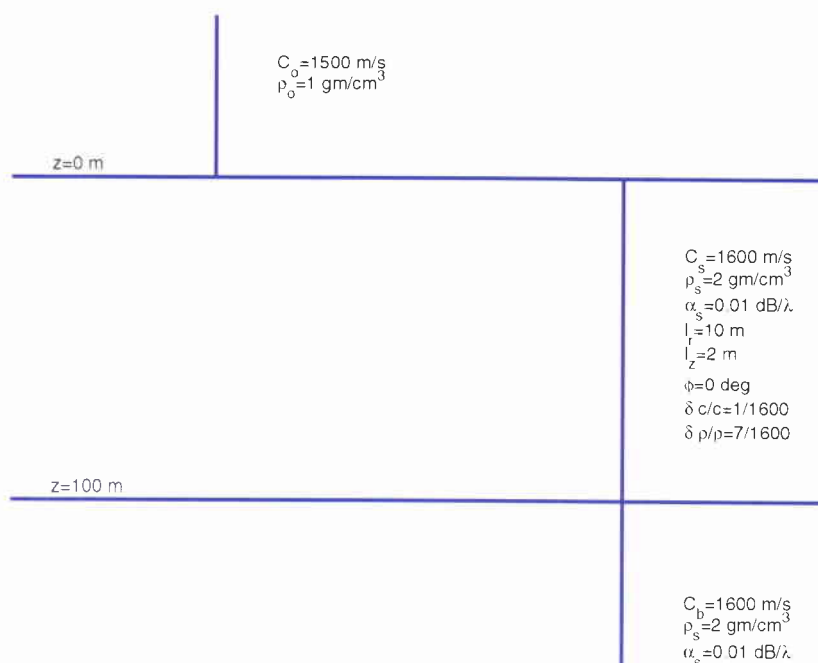


Figure 7 Scenario 2 is typical of a sandy sediment layer, with a sediment background sound speed of 1600 m/s, density of 2 g/cm³ and attenuation of 0.01 dB/ λ . The basement properties are identical to the background properties of the sediment, and the scatterer distribution properties are identical to those in Scenarios 1.

eled. Failings in the ray theory approximation to the Green functions are especially evident near turning points in refractive sediments and near the critical angle for fast sediments. Another significant advantage is that the spectral integral approach correctly includes the scattering response of scatterers which have been excited by evanescent, or non-propagating waves. This type of scattering is typically found in fast sediments along the sediment water interface at ranges where the incident angle of the source is smaller than the critical angle. For scatterers ensonified by these types of waves, the differential plane wave scattering cross section is undefined. Yet it is known that scatterers ensonified by these types of waves can be important contributors to the total scattered field [9]. In fact sub-critical penetration and scattering is the basis for advanced mine hunting sonar concepts for buried object detection [26, 27]. If this mechanism is going to be included for modeling target response, it is important that a similar mechanism be included for modeling the reverberation from sediment volume inhomogeneities, especially for smooth bottoms. For these reasons in Scenario 2 we compare the scattering predictions of the spectral integral approach to SCARAB for a fast sediment scattering scenario in order to evaluate the differences between the two approaches when there is a critical angle.

Scenario 2 is illustrated in Figure 7. A point source is situated 25 m above a fast

SACLANTCEN SM-376

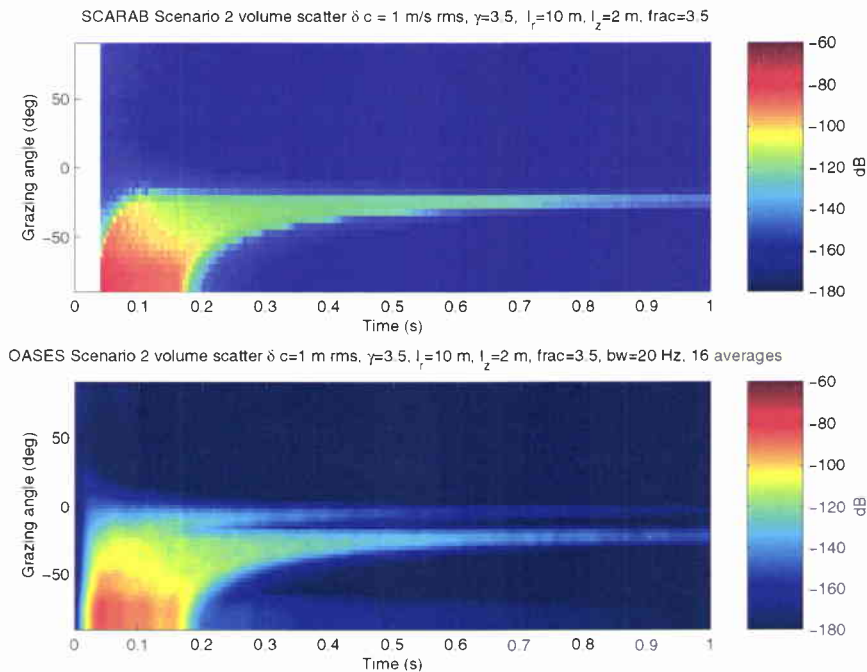


Figure 8 *The time-beam evolution of scattered intensity for Scenario 2. While the general agreement at angles greater than the critical angle is very good, the forced evanescent scattering branch following the time-angle trajectory of the sediment-water interface is missing in the SCARAB result (top.) This branch is seen in the spectral integral results (bottom) as well as the headwave scattering branch arriving at and above the critical angle of 20° . The presence of the fast sediment causes the scattering associated with the propagating part of the Green function to be confined to angles greater than or equal to the critical angle of the bottom for all times greater than the time necessary to interrogate the sediment layer at the critical angle, about 90 ms for the current geometry.*

sediment layer 100 m thick with a background sound speed of 1600 m/s, density of 2 g/cm^3 and attenuation of $0.01 \text{ dB}/\lambda$. In the sediment layer there is the similar distribution of 100% correlated sound speed and density fluctuations as were described in Scenario 1. The rms sound speed fluctuation is 1 m/s, the rms density fluctuation is $7/1600 \text{ g/cm}^3$ and the correlation length scales are $\ell_x = \ell_y = 10 \text{ m}$ and $\ell_z = 2 \text{ m}$. The source characteristics are the same as in Scenario 1.

In Figure 8 the time-angle evolution of backscattered intensity is illustrated for the fast sandy bottom type of Scenario 2. The SCARAB result is shown in the top plot and the spectral integral result is shown in the bottom plot. The results are in good agreement for angles greater than the critical angle of 20° , but the spectral integral result also shows a shallower angle branch at late time which conforms to the time-angle trajectory of the sediment water interface. This upper trace corresponds

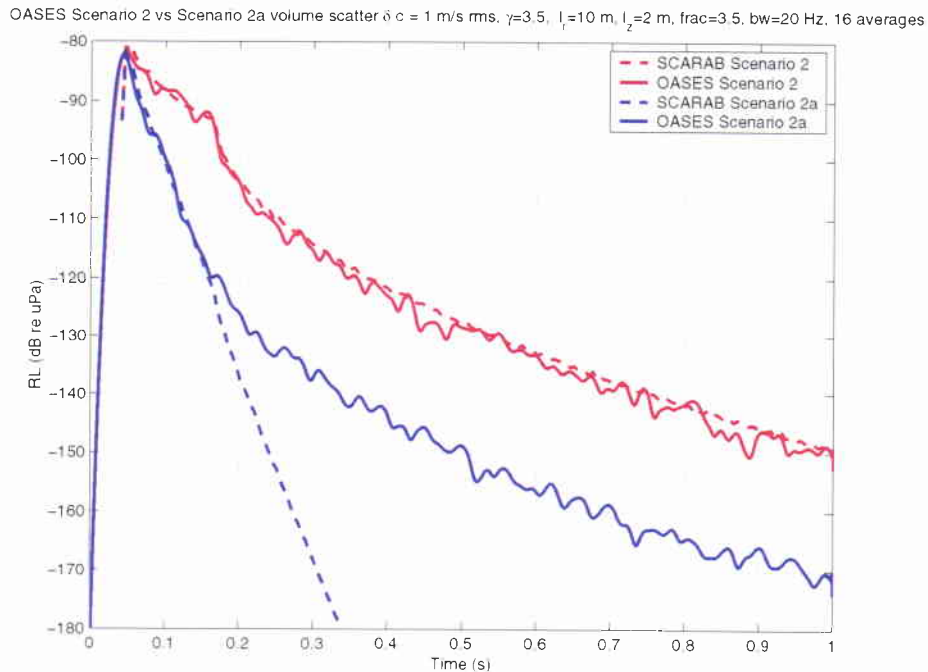


Figure 9 Single phone average intensity estimates for Scenario 2 (red) and Scenario 2a (blue) which has a higher sediment attenuation of 0.5 dB/ λ . The equivalent SCARAB predictions are indicated by the dashed lines of the appropriate color. The results show that in Scenario 2a the SCARAB and spectral integral results do not agree. This is due to the absence in SCARAB of an evanescent wave scattering mechanism.

to the inhomogeneous forcing of scatterers by non-propagating evanescent waves at the sediment water interface. Since the waves are not propagating in the sediment, there is no differential scattering cross section for SCARAB to use to estimate this branch. Instead SCARAB estimates that the only propagation path of importance to scatterers near the sediment water interface is the headwave path, which enters the sediment at the critical angle and propagates at near-horizontal angles to these scatterers and back. This is a fundamental limitation of the SCARAB assumption that all of the scattering of the sediment volume inhomogeneities can be parameterized in terms of differential scattering cross section.

In Figure 9 the scattered intensity received monostatically for Scenario 2 is illustrated in red. Here it is seen that although the SCARAB result neglects the inhomogeneous scattering mechanism, the overall agreement between the spectral integral result and SCARAB is quite good. This is because in this case the attenuation in the sediment, 0.01 dB/ λ , is sufficiently small that the headwave propagation path is the strongest contributor to the total scattered field for the times of interest in this simulation. However, in Scenario 2a when we increase the sediment attenuation to

SACLANTCEN SM-376

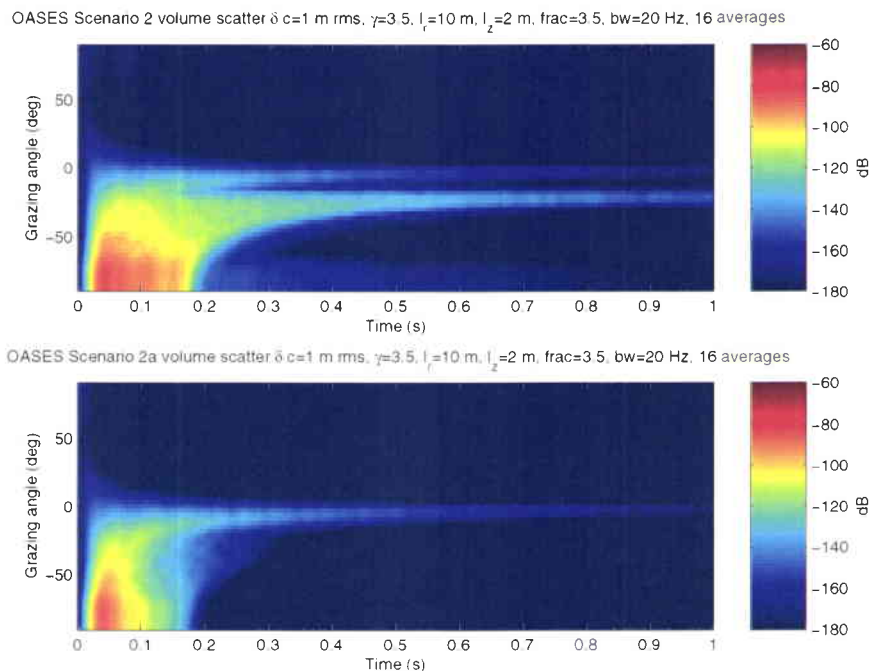


Figure 10 The time-beam evolution of scattered intensity for Scenario 2 (upper panel) and Scenario 2a (lower panel) which has a lossier sediment. In the lossier sediment case, the headwave scattering branch is attenuated after about 0.3 s. At times greater than this, the evanescent scattering path associated with the sediment water interface is the only scattering mechanism of importance.

0.5 dB/ λ , the blue curves show that SCARAB and the spectral integral result no longer agree for times later than about 0.16 s. This is due to the lack of an evanescent scattering mechanism in SCARAB. Taken together, the results for Scenarios 2 and 2a indicate that the evanescent scattering mechanism is about 20 dB down from the headwave mechanism in the absence of loss. For the sake of completeness, the beam time trajectories for Scenarios 2 and 2a are illustrated in Figure 10.

3.3 Scenario 3: Volume scattering from a upward refracting sediment layer

Gradients in the background properties of sediments are commonly observed in coring data and in bottom sound speed inversions [28, 29]. Gradients are important to the physics of the scattering process because they control how the subbottom is illuminated [4, 8]. These gradients are often composed of microstructure with significant sound speed and density variance. However, some of the characteristics of scattering from these types of sediments may be accounted for by assuming that the background properties are smoothly varying over the depth of the sediment layer.

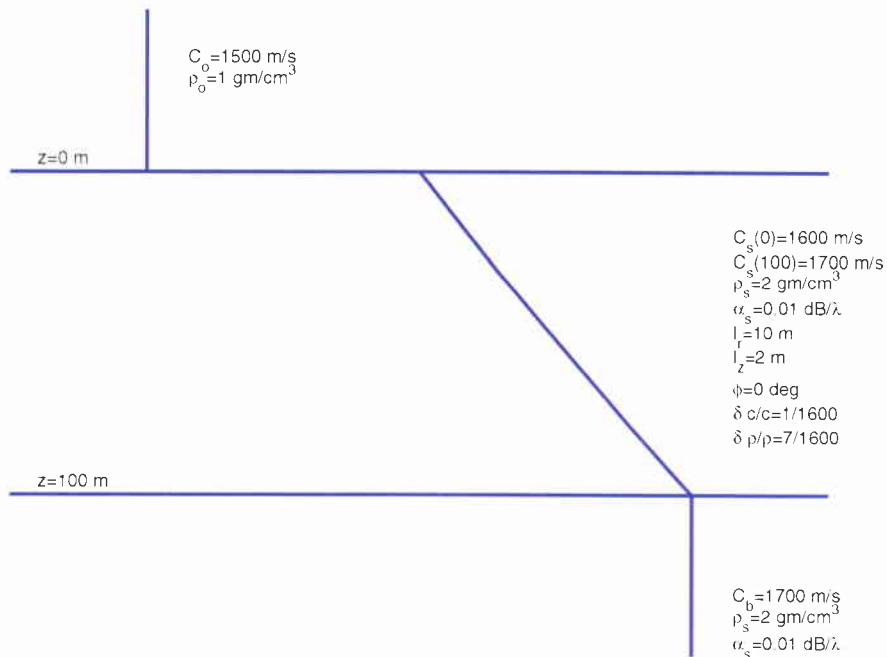


Figure 11 Scenario 3 is an upward refracting sandy sediment layer, with a sediment background sound speed of 1600 m/s at the sediment water interface, 1700 m/s at the sediment-basement interface, density of 2 g/cm³ and attenuation of 0.01 dB/ λ . The basement has a sound speed of 1700 m/s and has properties which are otherwise identical to those of the sediment layer. The scatterer distribution in the sediment layer are identical to those in Scenarios 2.

In spectral integral techniques, sound speed gradients which obey linearity in the square of the index of refraction may be handled exactly, as in these cases the depth separated wave equation becomes a differential equation whose solutions are Airy functions [4, 15]. In Scenario 3 such a gradient is introduced into the background sound speed properties of the fast sandy sediment in Scenario 2. The sound speed at the bottom of the layer is increased to 1700 m/s, while all the other properties of the sediment layer are held fixed. To eliminate multipath, the basement sound speed is also set at 1700 m/s.

The effect of the sound speed gradient on the incident field is illustrated in Figure 12, where the range-depth transmission loss is shown for the point source 25 m above the sediment water interface at 500 Hz for Scenarios 2 and 3. In both scenarios, the incident field passes unhindered into the sediment layer save for a small reflection loss for ranges up to 67 m, where the critical angle occurs. However in Scenario 2, the field then passes down into the lower halfspace, while in Scenario 3 a significant portion of the transmitted energy is refracted back up into the sediment layer.

SACLANTCEN SM-376

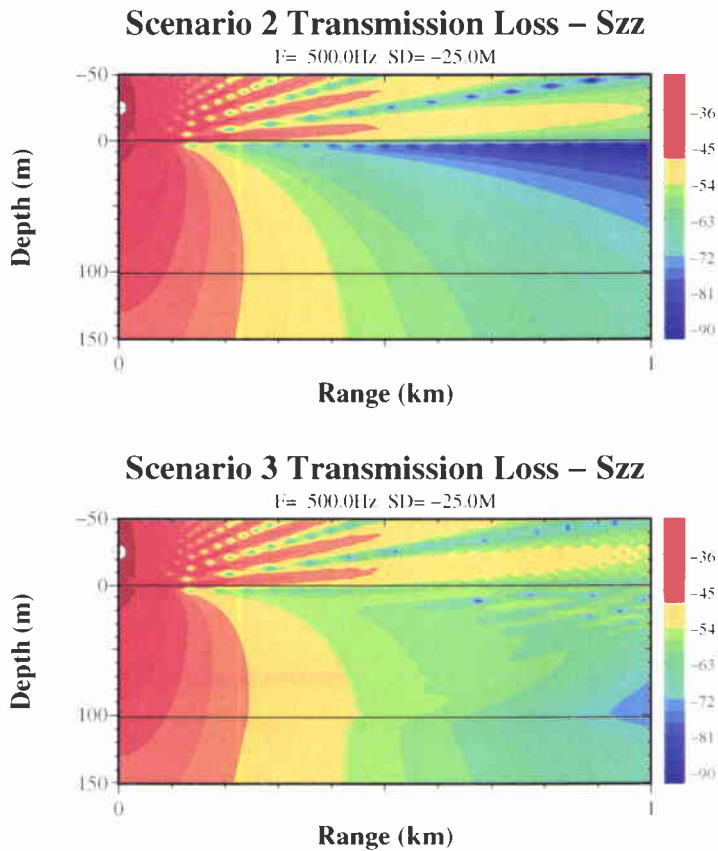


Figure 12 The range-depth transmission loss for Scenarios 2 (top) and 3 (bottom) at 500 Hz. In Scenario 2 the energy passing into the bottom above the critical angle passes through the sediment basement interface and is lost to the sediment layer. In Scenario 3 the upward refracting sediment sound speed causes a significant amount of the incident energy to be retained at longer ranges from the source.

In Figure 13 the time angle distributions of backscattered intensity for Scenarios 2 and 3 are shown. The results show that these distributions are significantly different. While the high angle early time backscatter and the forced inhomogeneous backscatter associated with the sediment water interface are identical for the two scenarios, the deep refracted or headwave path contains significantly more energy at late time for Scenario 3 than it does for Scenario 2. The angular width of the refracted scattering branch is also wider for Scenario 3, because higher angle energy is able to ensound the sediment layer at late times due to the refraction of this energy back into the sediment layer before it can escape into the basement.

In Figure 14 the backscattered intensity for the two scenarios is shown. Here it can be seen that the decay rate of the reverberation from the sediment volume inhomogeneous

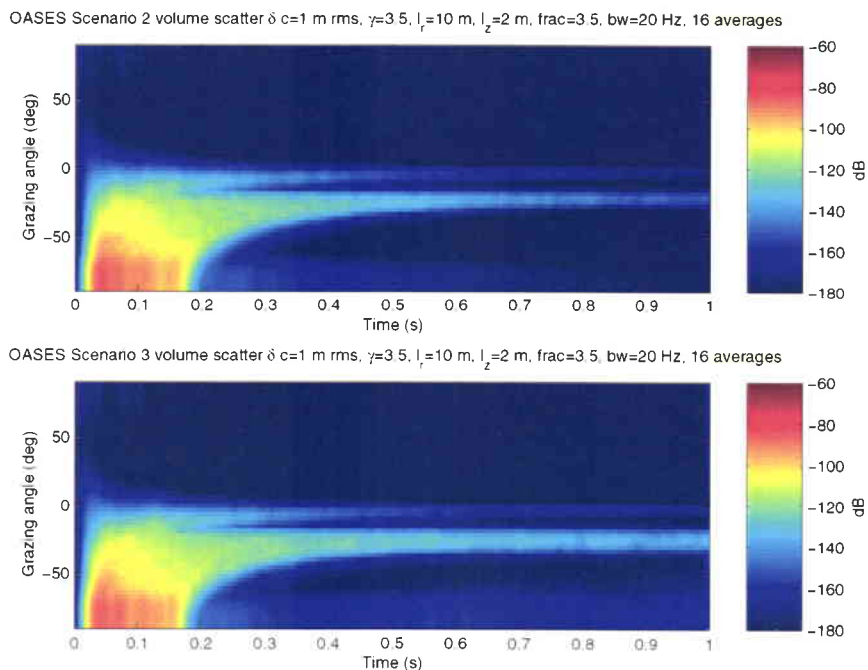


Figure 13 *Time-angle evolution of scattered intensity for the iso-speed fast bottom in Scenario 2 (upper plot) and the upward refracting sediment in Scenario 3 (lower plot.) The results for Scenario 3 indicate that upward refracting sediments can have significantly more late time reverberation over a broader range of grazing angles than otherwise similar sediment layers without gradients.*

genities in the upward refracting sediment in Scenario 3 is significantly slower than for the iso-speed sediment in Scenario 2. The implication is that sediment gradients can have a very significant effect on both the levels and the decay characteristics of sediment scattering.

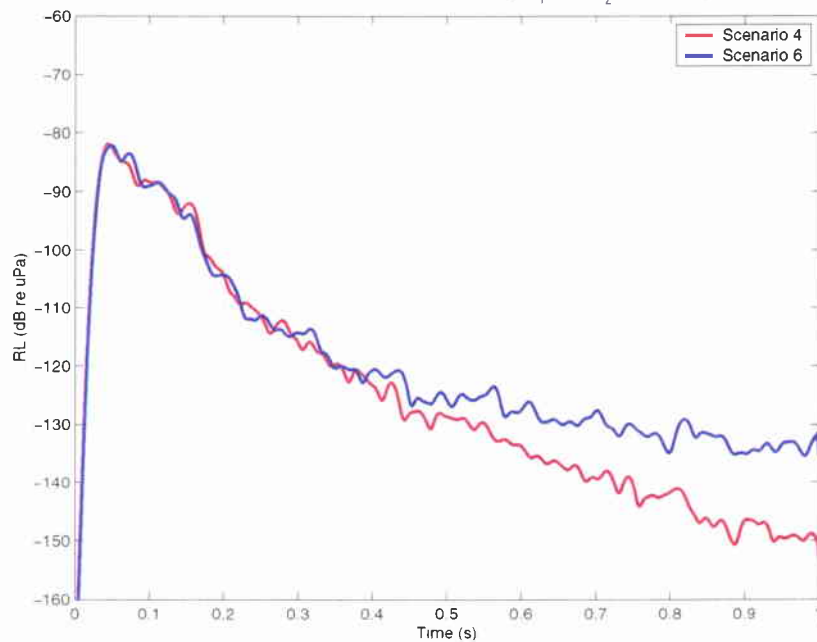
SACLANTCEN SM-376OASES Scenario 4 vs Scenario 6 volume scatter $\delta c = 1$ m/s rms, $\gamma=3.5$, $l_r=10$ m, $l_z=2$ m, frac=3.5, bw=20 Hz, 16 averages

Figure 14 *The scattered intensity received in a monostatic configuration for a fast sediment without a sound speed gradient (Scenario 2, red curve,) and a fast upward refracting sediment (Scenario 3, blue curve.) The results indicate that sediment gradients can have a very significant effect on scattered levels from sediment volume inhomogeneities at late time.*

4

Conclusions

The spectral integral representation for monostatic backscatter from three dimensional sediment inhomogeneities has been derived using the method of small perturbations and the Born approximation, and these equations have been implemented in a computationally efficient manner. The code offers the capability for “exactly” evaluating Monte-Carlo estimates of backscattered intensity and the time-angle evolution of backscattered intensity for sediment scenarios with critical angles and turning points under the perturbation and single scattering approximations. The potential also exists for treating sediment volume inhomogeneity scattering in more complicated bottoms by superimposing the single layer results derived and implemented here for all the contributing layers. For single layers, the results obtained here indicate that for slow sediments, the spectral integral estimates of backscattered intensity are in excellent agreement with those obtained by SCARAB using a simple sonar equation approach, as expected. However for fast and upward refracting sediments, the complete first order perturbation solution for the scattered field can only be obtained through the use of the spectral integral approach.

For fast sediments, it is found that a second scattering branch exists in the time-angle plane of scattered intensity. This second branch follows the time-angle evolution of scattering from the sediment-water interface, and is associated with the inhomogeneous excitation of the volume inhomogeneity scatterers closest to the sediment water interface. Since these scatterers are insonified by non-propagating waves, they have no defined farfield scattering cross section. Yet the results show that these scatterers can and do contribute to the backscattered signal in an important way. For inhomogeneities in fast smooth sediments with significant attenuation, this scattering mechanism is the only contributor to reverberation at late time.

For upward refracting sediments, we have shown that the intensification of the incident field on sediment inhomogeneities beyond the turning point of the basement grazing rays leads to increased backscattered levels at late time. This phenomenon is most likely to be observable in weakly lossy sediments, and can only be properly modeled near ray caustics with the wave theoretic approach used here.

The numerical implementation of a benchmarked spectral integral formalism for three dimensional sediment inhomogeneity scattering into the OASES framework makes it possible to evaluate the quality of the various approximations which are routinely

SACLANTCEN SM-376

taken for perturbation estimates of backscattered intensity from sediments. For instance, it is possible to evaluate the suitability of neglecting vertically correlated scatterers, or to evaluate when the evanescent scattering path mechanism may be appropriately neglected. It also makes it possible to evaluate the loss of fidelity associated with various approximations for evaluating the field near the critical angle for fast sediments or near the turning point in upward refracting sediments.

5

Acknowledgments

The authors wish to acknowledge Charles Holland, Peter Neumann and Andrew Rogers for supplying the SCARAB code and Ivar Bratberg for his assistance modifying and running it.

References

-
- [1] A. N. Ivakin and Y. P. Lysanov, "Theory of underwater sound scattering by random inhomogeneities of the bottom," *Sov. Phys. Acoust.* **27**, 61–64, (1981).
 - [2] A. N. Ivakin, "A unified approach to volume and roughness scattering," *J. Acoust. Soc. Am.* **103**, 827–837, (1998).
 - [3] D. Tang, *Acoustic Wave Scattering from a Random Ocean Bottom*, Doctoral Dissertation, MIT-WHOI Joint Program, WHOI-91-25, June 1991.
 - [4] P. D. Mourad and D. R. Jackson, "A model/data comparison for low frequency bottom backscatter," *J. Acoust. Soc. Am.* **94**, 344–358 (1993).
 - [5] B. H. Tracey and H. Schmidt, "A self-consistent theory for seabed volume scatter," *J. Acoust. Soc. Am.* **106**, 2524–2534 (1999).
 - [6] T. Yamamoto, "Acoustic scattering in the ocean from velocity and density fluctuations in the sediments," *J. Acoust. Soc. Am.* **99**, 866–879 (1996).
 - [7] A. Rogers and C. Holland, "SCARAB version 1.01, Users Manual," August 1997, Planning Systems Incorporated.
 - [8] C. W. Holland and P. Neumann, "Sub-bottom scattering: A modeling approach," *J. Acoust. Soc. Am.* **104**, 1363–1373 (1998).
 - [9] P. C. Hines, "Theoretical model of acoustic backscatter from a smooth seabed," *J. Acoust. Soc. Am.* **88**, 324–334, (1990).
 - [10] P. C. Hines, "Theoretical model of in-plane scatter from a smooth sediment seabed," *J. Acoust. Soc. Am.* **99**, 836–844, (1996).
 - [11] K. LePage and H. Schmidt, "Spectral integral representations of scattering from volume inhomogeneities," SM-363, SACLANT Undersea Research Centre, La Spezia, Italy (1999).
 - [12] H. Schmidt and J. Lee, "Physics of 3-D scattering from rippled seabeds and buried targets in shallow water," *J. Acoust. Soc. Am.* **105**, 1605–1617, (1999).
 - [13] H. Schmidt and K. D. LePage, "Spectral integral representations of multistatic scattering from sediment volume inhomogeneities," *J. Acoust. Soc. Am.* **108**, No. 5, Part 2, 2564, (2000).
 - [14] P. M. Morse and H. Feshbach, *Methods of Theoretical Physics*, Problem 7.9 (McGraw-Hill, New York, 1953.)

- [15] F.B. Jensen, W.A. Kuperman, M.B. Porter, and H. Schmidt, *Computational Ocean Acoustics*, (Springer-Verlag, 2000).
- [16] H. Schmidt and J. Glattetre, "A fast field model for three-dimensional wave propagation in stratified environments based on the global matrix method," *J. Acoust. Soc. Am.* **78**, 2105–2114 (1985).
- [17] H. Schmidt, "SAFARI: Seismo-acoustic fast field algorithm for range independent environments. User's Guide," SR-113, SACLANT Undersea Research Centre, La Spezia, Italy (1988).
- [18] I. S. Gradshteyn and I. M. Ryzhik, *Table of Integrals, Series and Products*, 6.522.3 (Academic Press, New York, 1980.)
- [19] A. Turgut, "Inversion of bottom/subbottom statistical parameters from acoustic backscatter data," *J. Acoust. Soc. Am.* **102**, 833–852 (1997).
- [20] J. A. Goff and T. H. Jordan, "Stochastic modeling of seafloor morphology: inversion of sea beam data for second order statistics", *J. Geophys. Res.* **93**, 13589–13608 (1988).
- [21] F. DiNapoli and R. Deavenport, "Theoretical and numerical Green's function solution in a plane multilayered medium", *J. Acoust. Soc. Am.*, **73** 92–105 (1980).
- [22] J. A. Ferrari, D. Perciante and A. Dubra, "Fast Hankel transform of n th order," *J. Opt. Soc Am. A*, **16** 2581–2582 (1999).
- [23] Q. H. Liu and W. C. Chew, "Applications of the conjugate gradient fast Fourier Hankel transfer method with an improved fast Hankel transform algorithm," *Radio Sci.*, **29** 1009–1022 (1994).
- [24] Q. H. Liu and Z. Q. Zhang, "Nonuniform fast Hankel transform (NUFHT) algorithm," *Appl. Opt.*, **38** 6705–6708 (1999).
- [25] M. Abramowitz and I.A. Stegun, "Handbook of Mathematical Functions", (Dover, New York, 1970)
- [26] A. Maguer, W. L. J. Fox, H. Schmidt, E. Pouliquen and E. Bovio, "Mechanisms for subcritical penetration into a sandy bottom: Experimental and modeling results," *J. Acoust. Soc. Am.* **107**, 1215–1225 (2000).
- [27] A. Maguer, E. Bovio, W. L. J. Fox and H. Schmidt, "*In situ* estimation of sediment sound speed and critical angle," *J. Acoust. Soc. Am.* **108**, 987–996 (2000).
- [28] C. W. Holland and J. Osler, "High resolution geoacoustic inversion in shallow water: A joint time and frequency domain technique," *J. Acoust. Soc. Am.* **107**, 1263–1279 (2000).

SACLANTCEN SM-376

- [29] C. W. Holland, R. Hollett and L. Troiano, "Measurement technique for bottom scattering in shallow water," *J. Acoust. Soc. Am.* **108**, 997–1011 (2000).

Annex A

Variance and covariance of Fourier-Bessel coefficients of scatterer distributions

A generalization of Eq. 13 gives the expression for the Fourier-Bessel coefficients of the scatterer distribution at depth z'

$$\begin{aligned} \tilde{\delta}c_m(p_r, z') &= \int dr \int dp'_r r p'_r J_m(p_r r) \int_0^{2\pi} d\theta' \tilde{\delta}c(p'_r \cos \theta', p'_r \sin \theta', z') \\ &\quad \times \int_0^{2\pi} d\theta \begin{Bmatrix} \cos(m\theta) \\ \sin(m\theta) \end{Bmatrix} e^{ip'_r r \cos(\theta' - \theta)}. \end{aligned} \quad (32)$$

The integral over θ may be evaluated yielding

$$\begin{Bmatrix} \cos(m\theta') \\ \sin(m\theta') \end{Bmatrix} J_m(p'_r r) = \int d\theta \begin{Bmatrix} \cos(m\theta) \\ \sin(m\theta) \end{Bmatrix} e^{ip'_r r \cos(\theta' - \theta)},$$

thus the expression for the expansion coefficient becomes

$$\begin{aligned} \tilde{\delta}c_m(p_r, z') &= \int dr \int dp'_r r p'_r J_m(p'_r r) J_m(p_r r) \\ &\quad \times \int_0^{2\pi} d\theta' \begin{Bmatrix} \cos(m\theta') \\ \sin(m\theta') \end{Bmatrix} \tilde{\delta}c(p'_r \cos \theta', p'_r \sin \theta', z'). \end{aligned} \quad (33)$$

For a homogeneous process with Gaussian amplitude distributions the spectral coefficients $\tilde{\delta}c(p_x, p_y)$ are independent circular Gaussian random variables with quadrature variances $\sigma_{\Re \tilde{\delta}c}^2(p_x, p_y) = \sigma_{\Im \tilde{\delta}c}^2(p_x, p_y) = P(p_x, p_y)$, where P is the power spectrum of the scatterer distributions. Using this knowledge, the variance of the azimuthal integral on the second line of Eq. 33 may be obtained as

$$\begin{aligned} &\int_0^{2\pi} d\theta' \int_0^{2\pi} d\theta \begin{Bmatrix} \cos(m\theta') \\ \sin(m\theta') \end{Bmatrix} \langle \tilde{\delta}c(p'_r \cos \theta', p'_r \sin \theta', z') \tilde{\delta}c^*(p'_r \cos \theta, p'_r \sin \theta, z') \rangle \begin{Bmatrix} \cos(m\theta) \\ \sin(m\theta) \end{Bmatrix}^\dagger \\ &= \int_0^{2\pi} d\theta' \int_0^{2\pi} d\theta \begin{Bmatrix} \cos(m\theta') \cos(m\theta) & \cos(m\theta') \sin(m\theta) \\ \sin(m\theta') \cos(m\theta) & \sin(m\theta') \sin(m\theta) \end{Bmatrix} P(p'_r \cos \theta, p'_r \sin \theta) \frac{\delta(\theta - \theta')}{p'_r} \\ &= \int_0^{2\pi} d\theta \begin{Bmatrix} \cos(m\theta) \cos(m\theta) & \cos(m\theta) \sin(m\theta) \\ \sin(m\theta) \cos(m\theta) & \sin(m\theta) \sin(m\theta) \end{Bmatrix} \frac{P(p'_r \cos \theta, p'_r \sin \theta)}{p'_r}. \end{aligned} \quad (34)$$

SACLANTCEN SM-376

If the scatterer distribution is isotropic, then $P(p'_r \cos \theta, p'_r \sin \theta) \equiv P(p_r)$, and if the distribution is real the quadrature components are conjugate symmetric so that the azimuthal integral on the last line of Eq. 34 may be evaluated to obtain the covariance

$$\begin{Bmatrix} 3 - \epsilon_m & 0 \\ 0 & \epsilon_m - 1 \end{Bmatrix} \pi \frac{P(p'_r)}{p'_r}. \quad (35)$$

Note that the covariance between the cos and sin terms of $\tilde{\delta}c_m$ are independent.

Using Eq. 35, Eq. 33 may be written as a Fourier-Bessel integral of a Gaussian distributed random variable with zero mean and variance given in Eq. 35

$$\begin{aligned} \tilde{\delta}c_m(p_r, z') &= \int dr \int dp'_r r p'_r J_m(p'_r r) J_m(p_r r) \\ &\times \begin{Bmatrix} 3 - \epsilon_m & 0 \\ 0 & (\epsilon_m - 1) \end{Bmatrix} \begin{Bmatrix} N\left(0, \pi \frac{P(p'_r)}{p'_r}\right) \\ N\left(0, \pi \frac{P(p'_r)}{p'_r}\right) \end{Bmatrix}, \end{aligned} \quad (36)$$

which according to the Fourier-Bessel integral relation [14] yields the identity

$$\tilde{\delta}c_m(p_r, z') = \begin{Bmatrix} 3 - \epsilon_m & 0 \\ 0 & \epsilon_m - 1 \end{Bmatrix} \begin{Bmatrix} N\left(0, \pi \frac{P(p_r)}{p_r}\right) \\ N\left(0, \pi \frac{P(p_r)}{p_r}\right) \end{Bmatrix}. \quad (37)$$

Finally, it should be noted that the covariance between the scatterer distribution coefficients of different orders is identically zero

$$\langle \tilde{\delta}c_m(p_r, z') \tilde{\delta}c_n(p_r, z') \rangle \equiv 0,$$

since the inner product of the differing harmonics of cos and sin are identically zero. This implies that realizations of the scattered field may be obtained with Eq. 18 by generating independent realizations of $\tilde{\delta}c_m(p_r, z')$ for the $n = 0$ harmonic, greatly reducing memory requirements.

Annex B

Expressions for scattered intensity used by SCARAB

The SCARAB model was developed to address deficiencies of many of the then existing bottom scattering models. Holland and Neumann [8] departing from the commonly-used local plane-wave approximation (which they showed was inadequate) by modeling the received level in the time domain with all of the experiment complexities, then calculated bottom scatter under exactly the same assumptions as the measured data were processed. This is the essence of the SCARAB model: to model as closely as possible the measurement conditions, including assumptions used in the data processing. Invoking the Born approximation, the received level from a single ping can be written as a sum of delayed, scaled, replicas of the transmit source intensity $S(t)$:

$$RL(T, \theta) = 10 \log \left[\sum_{i=1}^N S(t - t_i) 10^{TL_i^1/10} 10^{-TL_i^2/10} dP/d\Omega(\theta_i, z_i) \right] \quad (38)$$

where TL_i^1 and TL_i^2 are the transmission losses (including the beam pattern) from the source to scattering element i and from element i back to the receiver respectively. For sub-bottom volume scattering $dP/d\Omega$ is the differential scattering cross-section of a scatterer i at depth z ; N is the number of scatterers. In the initial version of the model used in [8], the propagation to and from the scatterers was computed using OASES and the scattering was calculated from randomly distributed 3D ellipsoids. A later version of the model employed a number of simplifications including use of ray theory for the propagation and replacing the scattering from randomly distributed deterministic scatterers with a stochastic approach. It is this simple version of the model that is used in the comparisons in this paper.

Document Data Sheet

Security Classification UNCLASSIFIED		Project No. 04-D
Document Serial No. SM-376	Date of Issue January 2001	Total Pages 38 pp.
Author(s) LcPage, K.D., Schmidt, H.		
Title Spectral integral representations of monostatic backscattering from three dimensional distributions of sediment volume inhomogeneities.		
Abstract A theory is developed for generating short time, monostatic reverberation realizations caused by three dimensionally distributed volume inhomogeneities in stratified media. A spectral integral approach to treating the propagation to an from the scatterers, combined with a two dimensional spectral representation of the azimuthally averaged scatterer realizations and a novel numerical implementation, combine to yield an efficient, high fidelity reverberation realization generator for predicting monostatic backscatter from realistic sediments.		
Keywords Reverberation – backscatter – volume scattering – seabed inhomogeneity		
Issuing Organization North Atlantic Treaty Organization SACLANT Undersea Research Centre Viale San Bartolomeo 400, 19138 La Spezia, Italy [From N. America: SACLANTCEN (New York) APO AE 09613]		Tel: +39 0187 527 361 Fax: +39 0187 527 700 E-mail: library@saclantc.nato.int

The SACLANT Undersea Research Centre provides the Supreme Allied Commander Atlantic (SACLANT) with scientific and technical assistance under the terms of its NATO charter, which entered into force on 1 February 1963. Without prejudice to this main task - and under the policy direction of SACLANT - the Centre also renders scientific and technical assistance to the individual NATO nations.

This document is approved for public release.
Distribution is unlimited

SACLANT Undersea Research Centre
Viale San Bartolomeo 400
19138 San Bartolomeo (SP), Italy

tel: +39 0187 527 (1) or extension
fax: +39 0187 527 700

e-mail: library@saclantc.nato.int

NORTH ATLANTIC TREATY ORGANIZATION